Degradations of Multijunction Solar Cell Revealed by Absolute Electroluminescence Imaging

Panpan Yang, Youyang Wang, Qiao Huang, Deyang Qin, Jianing Zhang, Wenjie Zhou [ID], Guoen Weng [ID], Xiaobo Hu [ID], Junhao Chu [ID], Hidefumi Akiyama, and Shaoqiang Chen [ID]

Abstract—Multijunction solar cells (MJSCs) experience material degradation and reduced efficiency during long-term storage. Current defect analysis methods for III–V compound MJSCs are limited by a lack of intuitive tools and in-depth understanding, hindering improvements in yield and efficiency. Absolute electroluminescence (EL) is a powerful technique for visualization and predicting solar cell performance. In this study, we applied absolute EL to quantify performance and degradation mechanisms in subcells after 26 months of storage. Absolute EL imaging identified both potential and inherent defect types within the subcells. The detailed analysis of localized defect points showed reduced photon emission near the defect points. Using the reciprocity theorem and carrier balance model, we found that degradation in the InGaP/GaAs/InGaAs solar cell resulted in a 0.8% reduction in efficiency, largely due to nonradiative recombination (NR) losses. Additionally, the efficiencies of top, middle, and bottom cells decreased by reduced by 0.3%, 0.2%, and 0.3%, respectively. This work demonstrates that the absolute EL imaging technique provides a comprehensive and detailed method for understanding defects and energy losses during long-term storage in MJSC.

Index Terms—Absolute electroluminescence (EL), degradation, GaAs, multijunction solar cells (MJSCs), nonradiative recombination (NR).

I. INTRODUCTION

RECENT advancements in photovoltaic technology have shifted focus from traditional single-junction solar cells to multijunction solar cells (MJSCs) [1], [2], [3], [4], [5], [6]. Unlike single-junction solar cells, MJSCs can convert a broader range of solar spectrum, surpassing the Shockley–Queisser (S–Q) efficiency limit and achieving efficiencies above 33% by stacking subcells [6], [7], [8]. Among them, III–V compound semiconductors, known for their high electron mobility and direct bandgap, have garnered significant attention [9], [10]. In parallel, flexible substrates are being developed through techniques, such as epitaxial lift-off (ELO) [11] and wafer bonding [12]. Currently, the highest efficiency for III–V compound triple-junction (3J) solar cells has reached 39.5% under AM1.5 global spectrum [13], achieved by optimizing the bandgap using strain-balanced quantum well in the middle cell. In particular, GaAs solar cells are critical for application in satellites [14], spacecraft [15], [16], [17], thermophotovoltaic [18], and semiconductor industry [19], [20]. These diverse applications highlight the importance of III–V compound MJSCs in the rapidly evolving landscape of photovoltaic devices.

Extending the lifespan and improving the conversion efficiency of III–V compound MJSCs are critical goals for their long-term development [21], [22], [23], [24]. Defect control is a key factor in the fabrication of solar cells, as defects can arise from various stages of manufacturing process [1], [25]. These defects originated from semiconductor synthesis [26], subcell fabrication, interface contact, and material lattice mismatching [27], [28], [29]. Several techniques, such as the gradient freeze technique [1], ELO [30], and rapid thermal annealing [31], have been developed to enhance performance by improving GaAs structural design and preparation. However, defects can also emerge during long-term storage, a factor often overlooked. Exposure to environmental elements, such as oxygen, moisture, high

temperature, and radiation [15], [32], [33], can accelerate material degradation, leading to more defects. One major issue caused by defects is nonradiative recombination (NR), which traps carriers and reduces device performance [34]. Defects can also worsen impurity diffusion, create poor contacts, and cause current leakage [35], [36], [37], further deteriorating the material and inducing more defects. While most studies on long-term storage of solar cells have focused on material [38] and overall device performance [39], [40], they typically span only a few months [41], leaving the long-term defect evolution unclear. It is essential to develop suitable methods for in-depth analysis of the defect changes in both individual subcells and entire MJSCs during long-term storage.

Electroluminescence (EL) measurement is a powerful technique for diagnosing and visualizing defects in solar cells [42], [43], [44]. Building on the previous works of Chen et al. [45] and Wang et al. [46], [47], the concept of absolute EL was introduced to overcome the limitations of relatively EL, enabling qualitative defect analysis through a distributed equivalent circuit model coupled with a set of detailed carrier balance equations. Absolute EL imaging allows for nondestructive testing of each subcell without the need to isolate or separately prepare single-junction devices. This technique not only helps in the understanding of traditional characteristics, such as current density–voltage (J–V) characteristics, but also predicts the change tendency of the device with corresponding computer simulations. However, there has been little research on the relationship between degradation and local or overall defects of MJSCs during long-term and nonoperational storage using absolute EL measurement. It is critical to apply defect characterization techniques to analyze how degradation impacts J–V characteristics and energy loss mechanisms, which can help assess the long-term reliability of these devices.

In this study, we conducted, for the first time, long-term defect tracking for the subcell degradation of a triple-junction solar cell over 26 months, predicting performance and explaining defects in the top cell and middle cell under prolonged storage. Absolute EL imaging revealed that some local defects present during fabrication worsened and became irreversible over time, while new defect types emerged gradually during long-term storage. As a result, the top, middle, and bottom cells with initial efficiencies of 17.4%, 11.8%, and 5.8%, respectively, experienced efficiency drops of 0.3%, 0.2%, and 0.3% over 26 months. Notably, NR losses increased significantly in each subcell and impacted more to the overall energy loss compared to other mechanisms. Therefore, NR loss is identified as the primary cause of performance degradation, rather than other energy loss pathways.

II. EXPERIMENTS AND EVALUATIONS

A. Basic Information About the 3J Solar Cell

As shown in Fig. 1(a), the 3J solar cell has a structure of InGaP/GaAs/InGaAs from the top cell to the bottom cell fabricated according to industry standards. The 3J solar cell
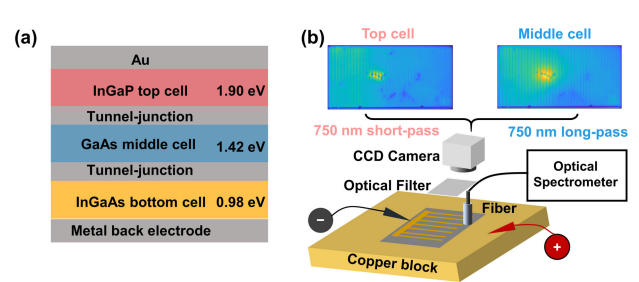

Fig. 1.　(a) Diagram structure of InGaP/GaAs/InGaAs 3J solar cell. (b) Schematic of absolute EL measurement.

is typically fabricated on GaAs substrate using metal–organic chemical vapor deposition (MOCVD) with the inverted metamorphic multijunction (IMMJ) process. The fabrication begins with the growth of the top InGaP cell, which is lattice-matched to the GaAs substrate, followed by the deposition of the GaAs middle cell and then a series of buffer layers with a gradually increasing indium (In) component to mitigate lattice mismatch. The bottom InGaAs cell is grown last on the buffer layers, followed by metal contact deposition. The epitaxy wafer is then mounted to a thin metal layer, and the GaAs substrate is removed. Finally, the front contact electrode and then the antireflection layer are fabricated on the top cell InGaP, forming a completed 3J solar cell [46]. We uniformly adopted storing 2 × 4 cm cells at dry cabinet with a humidity of 30% under dark conditions at room temperature. The test conditions use the same dark and dry conditions. From the first preparation, we store the 3J solar cell for up to 26 months in a nonworking state except for some necessary tests, including EL and other tests.

B. Characterization

As shown in Fig. 1(b), we present the schematic of absolute EL measurement, including monitoring computer, CCD camera (Hamamatsu C8484-05C), optical filter, copper base platform, fiber, spectrometer (Shamrock SR-303, Andor), and current–voltage source (Keithley 2400 source). Absolute EL testing utilizes the principle of reciprocity relation (5) [48], where the device operates in light-emitting diode (LED) mode under injected current. During this process, absolute EL images are captured using a camera sensitive to the corresponding wavelength range. These images are then converted into photon emissions (EMs), which are used to derive key parameters, such as the related I–V curve. The specific theoretical basis is elaborated in Section II-C. The sample was put on the copper base platform and affixed using a vacuum pump to ensure good contact. For electrical measurements, the positive and negative electrodes of the current–voltage source were connected to the 3J solar cell metal electrode and the copper base platform, respectively. Under dark conditions, EL imaging was captured for the top cell (InGaP) and middle cell (GaAs) using 750-nm short-pass and 750-nm long-pass optical filters, respectively. These filters were selected to isolate the EM wavelengths with central peaks at 653 nm for the top cell and 873 nm for the middle cell.

Due to technical limitations, EL imaging of the bottom cell (InGaAs) could not be recorded using the Si-based camera (sensitive range: 300–1150 nm). Unlike relatively EL testing, absolute EL testing requires calibration before measurements to ensure the accurate acquisition of absolute EL images [49]. The J–V measurement of the solar cells was performed using a solar simulator (Newport Xe-lamp) with a source meter (Keithley 2400) at 100 mW/cm^2, under AM1.5G illumination.

C. Solar Cell Evaluations

For the 3J solar cell, the external radiation efficiency (ERE$_i$) of the whole top ($i = 1$), middle ($i = 2$), and bottom ($i = 3$) cells based on the luminescent coupling (LC) process is defined by the following equation:

$$\text{ERE}_i = R_{\text{ext}\_i}/(R_{\text{ext}\_i} + R_{\text{ext}\_i \to i+1} + R_{\text{NR}\_i})$$
$$(i = 1, 2, \text{ and } 3) \quad (1)$$

where R_{ext_i} and R_{NR_i} denote the absolute EL intensity and NR loss rate for subcells, respectively, while $R_{\text{ext}\_i \to i+1}$ represents the radiative EM rate between subcells (i.e., LC). Furthermore, based on (1), we obtained the model

$$R_{\text{ext}\_i \to i+1} = n_i^2 \cdot R_{\text{ext}\_i}, \quad (n_{i+1} > n_i) \quad (2)$$

where n_i is the subcell refractive index of the absorbing layer. Based on the above equations, the carrier balance model under light conditions can be expressed as follows:

$$R_{\text{sun}\_i} + J_L/q + R_{\text{ext}\_i-1 \to i}$$
$$= R_{\text{ext}\_i} + R_{\text{ext}\_i \to i+1} + R_{\text{NR}\_i} = R_{\text{ext}\_i}/\text{ERE}_i \quad (3)$$

$$R_{\text{sun}\_i} = J_{\text{sun}\_i}/q = \int_{Eg}^{\infty} \text{EQE}_i(E) \cdot S_{\text{AM1.5G}}(E) dE \quad (4)$$

where J_L represents the output current density at working conditions, q is the electron charge, R_{sun_i} is the absorption rate of sunlight, $S_{\text{AM1.5G}}(E)$ represents the AM1.5G solar spectrum when the photon energy is E, and $\text{EQE}_i(E)$ is the external quantum efficiency of the subcells. These equations already present the reciprocity theorem between working modes of solar cells and LED [48]. The photoelectric reciprocity relationship is further introduced to establish the relationship between EL imaging and J–V characteristics in the following equation:

$$V_i(J) = \frac{KT}{q} \ln \frac{(J_{\text{sun}\_i} + J_L + q \cdot R_{\text{ext}\_i-1 \to i}) \cdot \text{ERE}_i(J_L)}{J_0}$$
$$(5)$$

where J_0, K, and T represent the radiance rate per unit area in terms of current density, Boltzmann's constant, and Kelvin temperature, respectively. In this experiment, we used 0.025 mA/cm^2 as the step size to obtain ERE$_i$. Through the above equations and derivations, the photoelectric generation and energy loss process can be described theoretically in the case of illumination and injection conditions. In addition, carrier balance models are suitable for the evaluation of overall and local photoelectric conversion processes. The analysis of local properties is particularly important given the nonuniformities that often occur during material fabrication process.
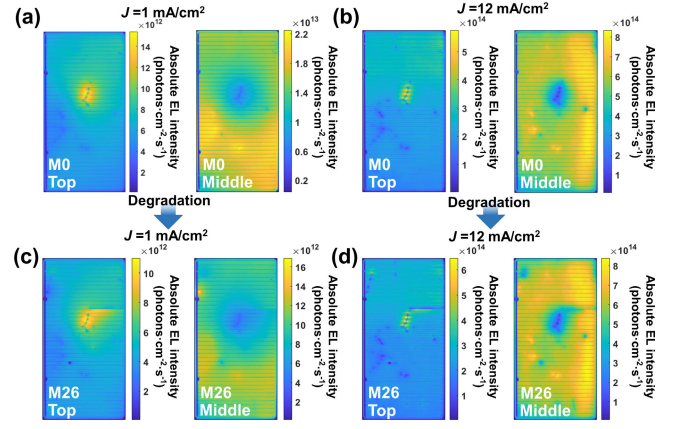

Fig. 2. EL imaging of top and middle cells in initial and 26 months under the injection current of (a) and (c) 1 mA/cm^2 and (b) and (d) 12 mA/cm^2.

III. RESULTS AND DISCUSSION

M0 and M26 represent the storage of the initial month (less than 1 month) and 26 months of 3J solar cell manufacturing, respectively. Fig. 2(a) and (c) shows the EL imaging of the top and middle cells at 1-mA/cm^2 injection current from the first month to 26 months. The EL imaging exhibited a light spot at the top cell and a dark spot at the middle cell, which indicated the area of defects expanded gradually. It can be observed that the same dark spots can be observed in the top and middle cells, which is due to the nonuniformity of the material resulting in defects throughout the different subcells. To compare the difference between small and large injection current conditions, we also adopted the same method under 12 mA/cm^2 shown in Fig. 2(b) and (d). As a result, the detailed distribution of individual defects under 12 mA/cm^2 is clearer than 1 mA/cm^2. It indicated a significant positive correlation between degradation degree and storage time.

To accurately evaluate the impact of storage time on degradation, defects are defined as potential and original types in Fig. 3. The emergence of potential defects occurs after 26 months, such as dot1 (d1) in the top cell and dot3 (d3) in the middle cell under 12 mA/cm^2. The original defects existed when the 3J solar cell was fabricated gradually expanded and deepened over time, such as dot2 (d2) and dot4 (d4) from the top and middle cell, respectively. Specifically, four defects (d1–d4) are randomly selected under the condition that they are not obscured by the gate electrode, ensuring that the selected defects are smaller in size and exhibit clearer characteristics. To further quantify the change of localized defect points in the subcell, we observed the change process of absolute EL in the red line region, where the four defects of d1–d4 are located along the y-direction (as blue line shown in the inset) in Fig. 4. The potential defects (d1, d3) remain essentially the same EL intensity as the nearby normal region at initial time (M0) and decrease more dramatically after 26 months. For the original defects (d2, d4), the decrease defects (d2, d4), the decrease in EL intensity after 26 months of degradation is not as pronounced. Overall, the degradation of each subcell can lead to a reduction in the number of emitted photons to some extent, and long-term storage has a greater impact on potential defects.
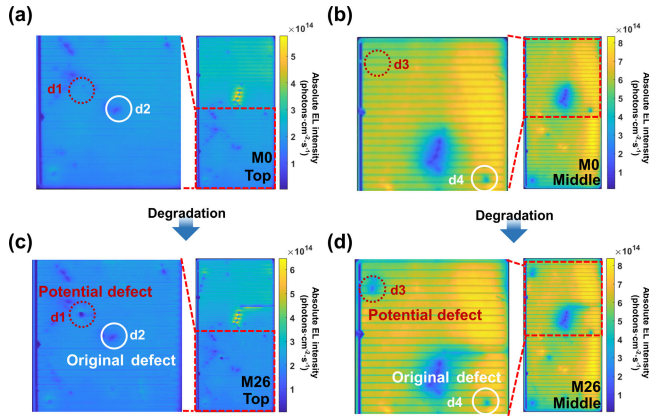
Fig. 3. Local and overall EL imaging of top cell in (a) M0 and (c) M26 and middle cell in (b) M0 and (d) M26 under 12 mA/cm² injection current.
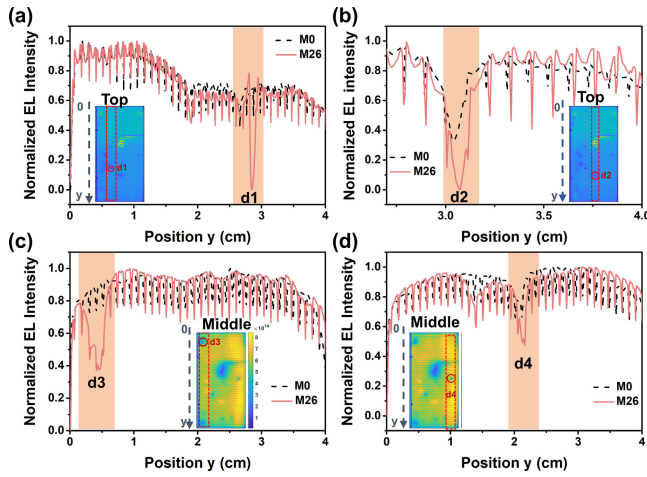

Fig. 4. Defect distributions of (a) and (b) top cell and (c) and (d) middle cell in the red dotted area follow the y-direction as the blue arrow in the inset.

We further investigated the spatial distribution characteristics of defects by integrating the EL intensity along the vertical direction of the subcell, according to the blue arrow direction in Fig. 4. Fig. 5(a) reveals a peak in the top cell and a valley in the bottom cell near 1.5 cm, observed both before and after long-term storage. These features correspond to a significant defect at this position, as highlighted in Fig. 2. Similarly, Fig. 5(b) also exhibits the same peaks and valleys under 12-mA/cm² injection. The difference is that the absolute EL intensity decreases slowly after long-term storage, which can be attributed to the saturation of the device's EM intensity at higher injection currents. Therefore, it is necessary to select a suitable injection current for a more comprehensive study of the defect characteristics of the device. In addition, the phenomenon that the maximum color bar of initial time [Fig. 2(b)] is higher than storage 26 months [Fig. 2(d)] in the top cell can be explained, which may be because long-term storage affects the local material properties and causes the defects to expand slightly. This slight increase in local EL intensity does not contradict the downward trend of the device's overall EL intensity in Fig. 5.
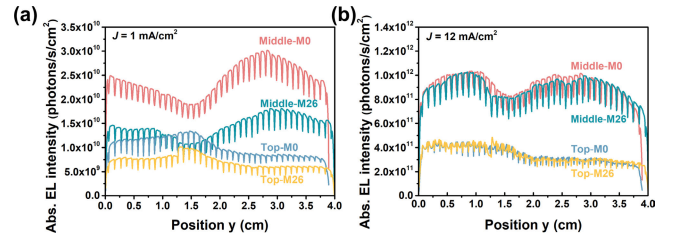

Fig. 5. Measured absolute EL distributions across the top and middle cells across the y-direction (as Fig. 4) under. (a) $J = 1$ mA/cm² and (b) $J = 12$ mA/cm².
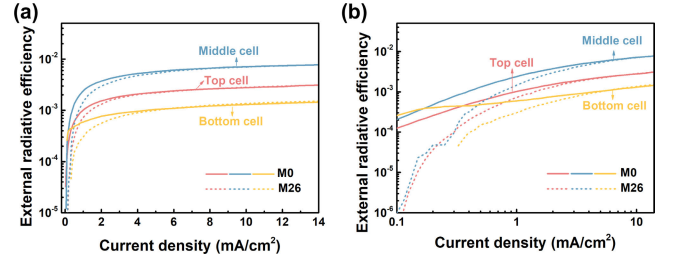

Fig. 6. Injection current density-dependent subcells EREs measured in M0 and M26 in (a) linear-log scale and (b) log–log scale.

Moreover, we are interested in exploring the impact of long-term storage on each subcell performance. According to (1), external radiation efficiency can effectively estimate the efficiency of the number of photons emitted in LED mode. The ERE in Fig. 6(a) depicts more photons being emitted upon high current injection, consistent with EL imaging in Fig. 2. However, from the log–log scale in Fig. 6(b), ERE produced an order of magnitude decrease after storage for 26 months between the top, middle, and bottom cells under low injection current density, corresponding to variation tendency in the overall spatial defect distribution via integrated to y-direction. The reason is that the number of emitted photons decreases under low injection current density and becomes relatively saturated with the increase of injection current density.

To evaluate the key parameters of the subcell and overall 3J solar cell, the $J{-}V$ curve of each subcell derived from the photoelectric reciprocity theorem [47] (5) was obtained under standard AM 1.5G illumination. As can be seen from Fig. 7(a), the efficiency of each subcell of the M26 group exhibited a decrease than the M0 group at maximum output power. Similarly, the efficiency of 3J solar cell exhibits degradation apparently after 26 months. Notably, while the Si-CCD (300–1150 nm) camera is unable to capture EL imaging from the bottom cell (InGaAs) ($E_g \sim 0.98$ eV and $\lambda_{abs} \sim 1265$ nm), the photon flux from the bottom cell can still be captured by a photodiode and converted into ERE, thereby obtaining the $J{-}V$ curve [49], [50], [51]. Furthermore, we also explored the degradation efficiency loss for the top, middle, bottom, and total cells in Table I for 0.3%, 0.2%, 0.3%, and 0.8%, respectively. In addition, referring to previous work, for different calibration methods, the absolute EL has an error of 10%–30% [50], [51]. Table I lists the efficiency errors caused by ±30% in EL intensity. The parameters of the device, including FF and V_{OC} for each subcell, were further analyzed and are shown in Fig. 7(b) and (c). FF and V_{OC} are

TABLE I
PERFORMANCE PARAMETERS OF SUBCELL AND TOTAL CELL FROM THE $J–V$ CURVE IN INITIAL AND 26 MONTHS UNDER THE CONDITION OF AM1.5G 1-SUN

Cell	J_{SC} (mA/cm²)	V_{OC} (V)	FF (%)	Efficiency (%)	Efficiency Error (%)
Top-M0	13.54	1.466	90.4	17.4	±0.12
Top-M26	13.54	1.465	89.0	17.1	±0.12
Middle-M0	13.98	1.008	89.1	11.8	±0.12
Middle-M26	13.98	1.009	87.2	11.6	±0.12
Bottom-M0	13.13	0.583	77.1	5.8	±0.09
Bottom-M26	13.13	0.584	72.3	5.5	±0.12
Total-M0	13.13	3.057	87.1	35.0	±0.26
Total-M26	13.13	3.059	85.2	34.2	±0.35

TABLE II
ENERGY LOSS OF SUBCELL AND TOTAL CELL AT INITIAL MONTH AT MAXIMUM OUTPUT POWER. ALL VALUES ARE PRESENTED IN THE FORM OF RATIOS

Cell	Input		Energy loss					Power Output
	AM 1.5G -sun	LC	TH loss	EM loss	LC	NR loss	JN loss	
Top	0.313	-	0.063	1.05E-5	1.28E-4	4.63E-3	0.072	0.174
Middle	0.224	1.28E-4	0.037	4.10E-5	5.02E-4	3.10E-3	0.065	0.118
Bottom	0.152	5.02E-4	0.023	1.06E-6	-	2.78E-3	0.068	0.058
TR loss	0.311	-	-	-	-	-	-	-
Total	1.000	6.31E-4	0.123	5.25E-5	6.31E-4	0.11	0.205	0.350

TABLE III
ENERGY LOSS PARAMETERS OF SUBCELL AND TOTAL CELL AFTER 26 MONTHS AT MAXIMUM OUTPUT POWER. ALL VALUES ARE PRESENTED IN THE FORM OF RATIOS

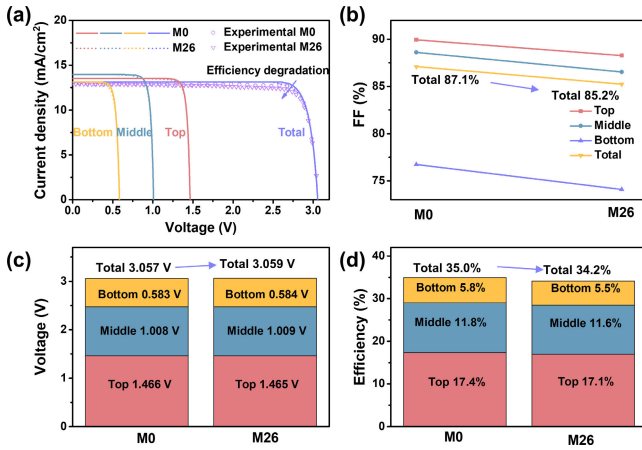| Cell	Input		Energy loss					Power Output
	AM 1.5G -sun	LC	TH loss	EM loss	LC	NR loss	JN loss	
Top	0.313	-	0.064	1.11E-5	1.36E-4	9.36E-3	0.069	0.171
Middle	0.224	1.36E-4	0.038	4.31E-5	5.28E-4	6.62E-3	0.063	0.116
Bottom	0.152	5.28E-4	0.024	7.49E-6	-	5.23E-3	0.067	0.055
TR loss	0.311	-	-	-	-	-	-	-
Total	1.000	6.64E-4	0.125	5.49E-5	6.64E-4	0.021	0.200	0.342

Fig. 7. (a) $J–V$ curve, (b) FF, (c) V_{OC}, and (d) efficiencies of each subcell and entire cell from M0 to M26 according to the photoelectric reciprocity theorem.
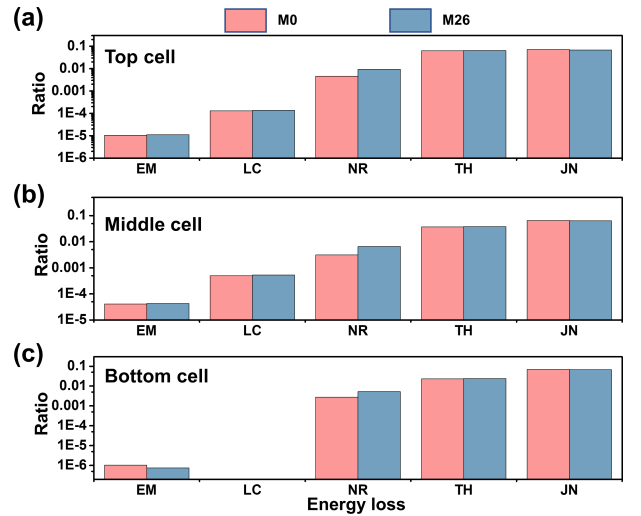

Fig. 8. Comparison of energy loss mechanism of (a) top, (b) middle, and (c) bottom cells from M0 to M26 degradation with operating at the maximum output power point.

87.1% and 3.057 V and 85.2% and 3.059 V for the M0 and M26 groups of total cells, respectively, and it can be observed that there is a significant decrease in the FF, reflecting device enhancement of parasitic resistance effects due to local shunt paths introduced by degradation.

From (1) to (5) and experimental data, the energy loss mechanisms were established to assess the impact of degradation on the solar cells after long-term storage. It is noted that the mechanisms of energy loss are complex and include radiative emission (EM) loss, NR loss, junction (JN) loss, thermal (TH) loss, LC loss, and transmission (TR) loss [45]. EM loss represents the energy by the absorber layer through radiative recombination. TH loss refers to the loss generated as heat energy. NR loss arises from material defects or NR centers, while JN loss is caused by the voltage drop between the bandgap energy (converted to V_{OC}) and the actual operating voltage of the device. LC loss is unique to MJSCs during the coupling of luminescent from an upper subcell to the subsequent lower subcell. Specifically, TH loss and JN loss were evaluated using EQE measurements and $J–V$ characteristics, respectively, while EM loss (from R_{ext_i}), LC loss (from R_{ext_i+1}), and NR loss (from R_{NR_i}) were derived from absolute EL measurement. TR loss refers to the energy that is not absorbed by the absorber layer and transmits

through the bottom cell [45], [47]. All energy loss ratios can be quantified when the solar cell operates at the maximum power conditions, as shown in Fig. 8 and Tables II and III [45]. For each subcell, the input is equal to the sum of the power output and energy losses. Notably, LC loss is absent in the bottom cell, as there is no LC from R_{ext_i+1} (LC = 0). It can be seen that the NR loss is the primary reason for the efficiency decrease, indicating that long-term storage can lead to serious NR loss, while EM, TH, JN, and LC losses exhibited a weak influence. Combined with the absolute EL measurement, original defects become more severe while potential defects are gradually exposed, leading to numerous NR centers and affecting the performance of the 3J solar cell.

IV. CONCLUSION

In summary, the degradation mechanism and performance of the 3J solar cell after 26 months of storage were analyzed using absolute EL combined with a CCD camera. Both overall and localized photon EMs were captured, revealing a decrease in total cell efficiency decreased from 35.0% to 34.2%. The efficiency reductions for the top, middle, bottom, and total cells were 0.3%, 0.2%, 0.3%, and 0.8%, respectively. This study highlights the role of different energy loss mechanisms in subcell performance degradation, with NR losses identified as the primary cause of device degradation after long-term storage. These findings offer valuable insights for future optimization of MJSCs, including material selection, process improvement, and sealing techniques.

REFERENCES

[1] J. Simon, C. Frank-Rotsch, K. Stolze, M. Young, M. A. Steiner, and A. J. Ptak, "GaAs solar cells grown on intentionally contaminated GaAs substrates," *J. Cryst. Growth*, vol. 541, Jul. 2020, Art. no. 125668, doi: 10.1016/j.jcrysgro.2020.125668.

[2] Y.-C. Kao et al., "Performance comparison of III–V//Si and III–V//InGaAs multi-junction solar cells fabricated by the combination of mechanical stacking and wire bonding," *Sci. Rep.*, vol. 9, no. 1, p. 4308, Mar. 2019, doi: 10.1038/s41598-019-40727-y.

[3] R. Wang, T. Huang, J. Xue, J. Tong, K. Zhu, and Y. Yang, "Prospects for metal halide perovskite-based tandem solar cells," *Nature Photon.*, vol. 15, no. 6, pp. 411–425, Jun. 2021, doi: 10.1038/s41566-021-00809-8.

[4] D. Zhao et al., "Efficient two-terminal all-perovskite tandem solar cells enabled by high-quality low-bandgap absorber layers," *Nature Energy*, vol. 3, no. 12, pp. 1093–1100, Nov. 2018, doi: 10.1038/s41560-018-0278-x.

[5] T. Ameri, N. Li, and C. J. Brabec, "Highly efficient organic tandem solar cells: A follow up review," *Energy Environ. Sci.*, vol. 6, no. 8, p. 2390, 2013, doi: 10.1039/c3ee40388b.

[6] G. E. Eperon, M. T. Hörantner, and H. J. Snaith, "Metal halide perovskite tandem and multiple-junction photovoltaics," *Nature Rev. Chem.*, vol. 1, no. 12, p. 95, Nov. 2017, doi: 10.1038/s41570-017-0095.

[7] S. Essig et al., "Raising the one-sun conversion efficiency of III–V/Si solar cells to 32.8% for two junctions and 35.9% for three junctions," *Nature Energy*, vol. 2, no. 9, p. 17144, Aug. 2017, doi: 10.1038/nenergy.2017.144.

[8] J. F. Geisz et al., "Building a six-junction inverted metamorphic concentrator solar cell," *IEEE J. Photovolt.*, vol. 8, no. 2, pp. 626–632, Mar. 2018, doi: 10.1109/JPHOTOV.2017.2778567.

[9] E. Aydin et al., "Enhanced optoelectronic coupling for perovskite/silicon tandem solar cells," *Nature*, vol. 623, no. 7988, pp. 732–738, Nov. 2023, doi: 10.1038/s41586-023-06667-4.

[10] M. A. Steiner et al., "32.9% efficient tandem solar cell with strain-balanced GaInAs/GaAsP quantum wells," in *Proc. IEEE 48th Photovoltaic Specialists Conf. (PVSC)*, Jun. 2021, pp. 1084–1085, doi: 10.1109/PVSC43889.2021.9518819.

[11] A. T. J. van Niftrik, J. J. Schermer, G. J. Bauhuis, P. Mulder, P. K. Larsen, and J. J. Kelly, "A diffusion and reaction related model of the epitaxial lift-off process," *J. Electrochem. Soc.*, vol. 154, no. 11, p. D629, 2007, doi: 10.1149/1.2779968.

[12] P. Dai et al., "The investigation of wafer-bonded multi-junction solar cell grown by MBE," *J. Cryst. Growth*, vol. 515, pp. 16–20, Jun. 2019, doi: 10.1016/j.jcrysgro.2019.02.064.

[13] R. M. France et al., "Triple-junction solar cells with 39.5% terrestrial and 34.2% space efficiency enabled by thick quantum well superlattices," *Joule*, vol. 6, no. 5, pp. 1121–1135, 2022, doi: 10.1016/j.joule.2022.04.024.

[14] M. Yamaguchi, T. Takamoto, K. Araki, and N. Ekins-Daukes, "Multi-junction III–V solar cells: Current status and future potential," *Sol. Energy*, vol. 79, no. 1, pp. 78–85, Jul. 2005, doi: 10.1016/j.solener.2004.09.018.

[15] R. H. van Leest et al., "Effects of copper diffusion in gallium arsenide solar cells for space applications," *Sol. Energy Mater. Sol. Cells*, vol. 140, pp. 45–53, Sep. 2015, doi: 10.1016/j.solmat.2015.03.020.

[16] A. LaPotin et al., "Thermophotovoltaic efficiency of 40%," *Nature*, vol. 604, no. 7905, pp. 287–291, Apr. 2022, doi: 10.1038/s41586-022-04473-y.

[17] P. T. Chiu et al., "Qualification of 32% BOL and 28% EOL efficient XTE solar cells," in *Proc. IEEE 46th Photovoltaic Spec. Conf. (PVSC)*, Jun. 2019, pp. 1506–1509, doi: 10.1109/PVSC40753.2019.8981370.

[18] C. Algora et al., "Beaming power: Photovoltaic laser power converters for power-by-light," *Joule*, vol. 6, no. 2, pp. 340–368, Feb. 2022, doi: 10.1016/j.joule.2021.11.014.

[19] I. Massiot, A. Cattoni, and S. Collin, "Progress and prospects for ultrathin solar cells," *Nature Energy*, vol. 5, no. 12, pp. 959–972, Nov. 2020, doi: 10.1038/s41560-020-00714-4.

[20] F. Dimroth et al., "Wafer bonded four-junction GaInP/GaAs//GaInAsP/GaInAs concentrator solar cells with 44.7% efficiency," *Prog. Photovolt., Res. Appl.*, vol. 22, no. 3, pp. 277–282, Mar. 2014, doi: 10.1002/pip.2475.

[21] M. A. Green et al., "Solar cell efficiency tables (version 61)," *Prog. Photovolt., Res. Appl.*, vol. 31, no. 1, pp. 3–16, Jan. 2023, doi: 10.1002/pip.3646.

[22] J. F. Geisz et al., "Six-junction III–V solar cells with 47.1% conversion efficiency under 143 suns concentration," *Nature Energy*, vol. 5, no. 4, pp. 326–335, Apr. 2020, doi: 10.1038/s41560-020-0598-5.

[23] V. Sharma and S. S. Chandel, "Performance and degradation analysis for long term reliability of solar photovoltaic systems: A review," *Renew. Sustain. Energy Rev.*, vol. 27, pp. 753–767, Nov. 2013, doi: 10.1016/j.rser.2013.07.046.

[24] M. Yamaguchi, "III–V compound multi-junction solar cells: Present and future," *Sol. Energy Mater. Sol. Cells*, vol. 75, nos. 1–2, pp. 261–269, Jan. 2003, doi: 10.1016/s0927-0248(02)00168-x.

[25] C. Leon, S. Le Gall, M.-E. Gueunier-Farret, and J.-P. Kleider, "How to perform admittance spectroscopy and DLTS in multijunction solar cells," *Sol. Energy Mater. Sol. Cells*, vol. 240, Jun. 2022, Art. no. 111699, doi: 10.1016/j.solmat.2022.111699.

[26] X. Pan, M.-Q. Yang, X. Fu, N. Zhang, and Y.-J. Xu, "Defective TiO$_2$ with oxygen vacancies: Synthesis, properties and photocatalytic applications," *Nanoscale*, vol. 5, no. 9, pp. 3601–3614, 2013, doi: 10.1039/c3nr00476g.

[27] C. G. Zimmermann, "Photoluminescence-based detection of mechanical defects in multijunction solar cells," *J. Appl. Phys.*, vol. 126, no. 4, Jul. 2019, Art. no. 044503, doi: 10.1063/1.5106414.

[28] L. Duan and A. Uddin, "Defects and stability of perovskite solar cells: A critical analysis," *Mater. Chem. Frontiers*, vol. 6, no. 4, pp. 400–417, Feb. 2022, doi: 10.1039/d1qm01250a.

[29] A. Baiju and M. Yarema, "Status and challenges of multi-junction solar cell technology," *Frontiers Energy Res.*, vol. 10, Sep. 2022, Art. no. 971918, doi: 10.3389/fenrg.2022.971918.

[30] P. Ramu et al., "Epitaxial lift-off process for GaAs solar cells controlled by InGaAs internal sacrificial stressor layers and a PMMA surface stressor," *Sol. Energy Mater. Sol. Cells*, vol. 248, Dec. 2022, Art. no. 111982, doi: 10.1016/j.solmat.2022.111982.

[31] M. Kim, Y. Sun, R. D. Hool, and M. L. Lee, "Metamorphic front- and rear-junction 1.7 eV GaInP solar cells with high open-circuit voltage," *Sol. Energy Mater. Sol. Cells*, vol. 259, Aug. 2023, Art. no. 112435, doi: 10.1016/j.solmat.2023.112435.

[32] M. Schmidt, D. Braunger, R. Schäffler, H. W. Schock, and U. Rau, "Influence of damp heat on the electrical properties of Cu(in,Ga)Se$_2$ solar cells," *Thin Solid Films*, vols. 361–362, pp. 283–287, Feb. 2000, doi: 10.1016/s0040-6090(99)00820-2.

[33] G. Gaspar et al., "Identification of defects causing performance degradation of high temperature n-type Czochralski silicon bifacial solar cells," *Sol. Energy Mater. Sol. Cells*, vol. 153, pp. 31–43, Aug. 2016, doi: 10.1016/j.solmat.2016.04.008.

[34] M. Yamaguchi, K. Araki, N. Kojima, and Y. Ohshita, "Overview and loss analysis of high-efficiency III-V compound single-junction solar cells," in *Proc. 47th IEEE Photovoltaic Spec. Conf. (PVSC)*, Jun. 2020, pp. 149–151, doi: 10.1109/pvsc45281.2020.9300850.

[35] H. Nesswetter, P. Lugli, A. W. Bett, and C. G. Zimmermann, "Electroluminescence and photoluminescence characterization of multijunction solar cells," *IEEE J. Photovolt.*, vol. 3, no. 1, pp. 353–358, Jan. 2013, doi: 10.1109/JPHOTOV.2012.2213801.

[36] L. Kong et al., "Performance evaluation of multi-junction solar cells by spatially resolved electroluminescence microscopy," *Nanosc. Res. Lett.*, vol. 10, no. 1, p. 40, Dec. 2015, doi: 10.1186/s11671-014-0719-9.

[37] L. Zhu et al., "Current leakage and fill factor in multi-junction solar cells linked via absolute electroluminescence characterization," in *Proc. IEEE 43rd Photovoltaic Spec. Conf. (PVSC)*, Jun. 2016, pp. 1239–1243, doi: 10.1109/PVSC.2016.7749812.

[38] Y.-C. Jung, Y.-J. Yu, Y.-K. Kim, J. H. Lee, J. H. Seo, and J.-Y. Choi, "Asymmetric TMO–metal–TMO structure for enhanced efficiency and long-term stability of Si-based heterojunction solar cells," *Materials*, vol. 16, no. 16, p. 5550, Aug. 2023, doi: 10.3390/ma16165550.

[39] E. L. Meyer and E. E. van Dyk, "Assessing the reliability and degradation of photovoltaic module performance parameters," *IEEE Trans. Rel.*, vol. 53, no. 1, pp. 83–92, Mar. 2004, doi: 10.1109/tr.2004.824831.

[40] L. Zhu et al., "Characterizations of radiation damage in multijunction solar cells focused on subcell internal luminescence quantum yields via absolute electroluminescence measurements," *IEEE J. Photovolt.*, vol. 6, no. 3, pp. 777–782, May 2016, doi: 10.1109/JPHOTOV.2016.2540247.

[41] B.-W. Park et al., "Long-term chemical aging of hybrid halide perovskites," *Nano Lett.*, vol. 19, no. 8, pp. 5604–5611, Aug. 2019, doi: 10.1021/acs.nanolett.9b02142.

[42] X. Jiang, C. Wang, X. Wang, Y. Zong, and C. Pei, "Defects detection in crystalline silicon solar cells based on electroluminescence imaging," *Proc. SPIE*, vol. 8193, pp. 315–321, Sep. 2011, doi: 10.1117/12.899581.

[43] D.-M. Tsai, S.-C. Wu, and W.-C. Li, "Defect detection of solar cells in electroluminescence images using Fourier image reconstruction," *Sol. Energy Mater. Sol. Cells*, vol. 99, pp. 250–262, Apr. 2012, doi: 10.1016/j.solmat.2011.12.007.

[44] V. E. Puranik and R. Gupta, "Standardized applications of electroluminescence imaging for efficient investigation of potential-induced degradation shunting in crystalline silicon photovoltaic module," *Sol. Energy*, vol. 245, pp. 183–192, Oct. 2022, doi: 10.1016/j.solener.2022.09.014.

[45] S. Chen et al., "Thorough subcells diagnosis in a multi-junction solar cell via absolute electroluminescence-efficiency measurements," *Sci. Rep.*, vol. 5, no. 1, p. 7836, Jan. 2015, doi: 10.1038/srep07836.

[46] Y. Wang et al., "Adaptive automatic solar cell defect detection and classification based on absolute electroluminescence imaging," *Energy*, vol. 229, Aug. 2021, Art. no. 120606, doi: 10.1016/j.energy.2021.120606.

[47] Y. Wang et al., "Defect-induced current coupling in multi-junction solar cells revealed by absolute electroluminescence imaging," *Prog. Photovolt., Res. Appl.*, vol. 30, no. 12, pp. 1410–1422, Dec. 2022, doi: 10.1002/pip.3601.

[48] U. Rau, "Reciprocity relation between photovoltaic quantum efficiency and electroluminescent emission of solar cells," *Phys. Rev. B, Condens. Matter*, vol. 76, no. 8, Aug. 2007, Art. no. 085303, doi: 10.1103/physrevb.76.085303.

[49] X. Hu et al., "Absolute electroluminescence imaging diagnosis of GaAs thin-film solar cells," *IEEE Photon. J.*, vol. 9, no. 5, pp. 1–9, Oct. 2017, doi: 10.1109/JPHOT.2017.2731800.

[50] A. Freundlich et al., "Calibration standards and measurement accuracy of absolute electroluminescence and internal properties in multi-junction and arrayed solar cells," *Proc. SPIE*, vol. 9743, pp. 40–45, Mar. 2016, doi: 10.1117/12.2211726.

[51] M. Yoshita et al., "Accuracy evaluations for standardization of multi-junction solar-cell characterizations via absolute electroluminescence," in *Proc. IEEE 43rd Photovoltaic Spec. Conf. (PVSC)*, Jun. 2016, pp. 3570–3573, doi: 10.1109/PVSC.2016.7750337.